Antichiral edge states in Heisenberg ferromagnet on a honeycomb lattice

Dhiman Bhowmick and Pinaki Sengupta
School of Physical and Mathematical Sciences, Nanyang Technological University, Singapore 637371, Singapore

(Received 2 July 2019; revised manuscript received 25 September 2019; accepted 13 April 2020; published 19 May 2020)

We demonstrate the emergence of antichiral edge states in a Heisenberg ferromagnet with Dzyaloshinskii-Moriya interaction (DMI) on a honeycomb lattice with inequivalent sublattices, using both Schwinger-boson mean field theory and Holstein-Primakoff transformation. The DMI, which acts between atoms of the same species, differs in magnitude for the two sublattices, resulting in a shifting of the energy of the magnon bands (or bands in each spinon sector) in opposite directions at the two Dirac points. The chiral symmetry is broken and, for sufficiently strong asymmetry, the band shifting leads to antichiral edge states (in addition to the normal chiral edge states) in a rectangular strip where the magnon (or up or down spinon) current propagates in the same direction along the two edges. This is compensated by a counterpropagating bulk current that is enabled by the broken chiral symmetry. We analyze the resulting magnon (spinon) current profile across the width of the system in details and suggest realistic experimental probes to detect them. Finally, we discuss possible materials that can potentially exhibit such antichiral edge states.

DOI: 10.1103/PhysRevB.101.195133

I. INTRODUCTION

Quantum magnets have emerged as a versatile platform for realizing magnetic analogs of the plethora of topological phases that have been predicted, analyzed, classified, and observed in electronic systems over the past decade. Haldane's paradigmatic model [1] of tight binding electrons on a honeycomb lattice with complex next-nearest-neighbor hopping—that constitutes the foundation of many of the electronic topological phases—has a natural realization in (quasi-)2D insulating ferromagnets such as CrI_3 [2] and $AFe_2(PO_4)_2$ (A=Ba,Cs,K,La) [3]. In many of these materials, the dominant Heisenberg exchange is supplemented by a next-nearest-neighbor antisymmetric DMI. These systems are described by two species of quasiparticles—spinons with up and down spins. The Kane-Mele-Haldane model—analogous to the Kane Mele model for electrons—has been proposed to describe the spinons over a wide range of temperatures [4]. The spinon bands acquire a nontrivial dispersion due to Berry phase arising from the DMI. This results in a spin Nernst effect (SNE), where a thermal gradient drives a transverse spin current, a spinon version of the spin Hall effect [4–7]. In a finite sample, the two spinon species generate two counterpropagating spin currents along the edges that are protected by chiral symmetry of the Hamiltonian—analogous to two copies of the thermal Hall effect (THE) of magnons that has been observed in many insulating magnets [8–11].

Recently, there has been growing interest in engineering systems with copropagating edge currents [12–14], through an ingenious, yet physically unrealistic, modification of the Haldane model. The conservation of net current is satisfied by counterpropagating bulk current. That is, the bulk is not insulating, in contrast to conventional topological insulators. In this work, we demonstrate that antichiral states arise naturally in spinons on a honeycomb magnet comprised of two different magnetic ions, with unequal DMI for the two sublattices. In the absence of DMI, the spinon dispersion consists of two doubly degenerate bands with linear band crossings at **K** and **K′** [15]. A finite DMI lifts the degeneracy between the two spinon branches and opens up a gap in the spectrum [16–19]. For *asymmetric* DMI, the two bands for each spinon species are shifted in opposite directions relative to each other at the **K** and **K′** points in the Brillouin zone. This results in similar dispersion for the gapless modes at both edges, giving rise to copropagating edge states. This is shown to yield effective antichiral edge states for the spinons in addition to normal chiral ones. We present a detailed characterization of the nature of the edge and bulk spinon states and suggest suitable experimental signatures to detect these topological states.

II. MODEL

We consider a Heisenberg ferromagnet on the honeycomb lattice with unequal DMI (D_A and D_B) on the two sublattices. Introducing the symmetric and antisymmetric combinations of D_A and D_B as $D = \frac{1}{2}(D_A + D_B)$ and $D' = \frac{1}{2}(D_A - D_B)$—termed chiral and antichiral DMI respectively for reasons that will become clear later—the Hamiltonian is given by

$$\mathcal{H} = -J\sum_{\langle i,j\rangle}\mathbf{S}_i\cdot\mathbf{S}_j + D\sum_{\langle\langle i,j\rangle\rangle}\nu_{ij}\hat{z}\cdot(\mathbf{S}_i\times\mathbf{S}_j) + D'\sum_{\langle\langle i,j\rangle\rangle}\nu'_{ij}\hat{z}\cdot(\mathbf{S}_i\times\mathbf{S}_j) - B\sum_i S_i^z, \quad (1)$$

where $J > 0$ is the nearest-neighbor Heisenberg interaction and $\nu_{ij} = +1$ when i and j are along the cyclic arrows shown in Fig. 1(b). Again, $\langle\ldots\rangle$ and $\langle\langle\ldots\rangle\rangle$ denote the nearest-neighbor and next-nearest-neighbor bonds,

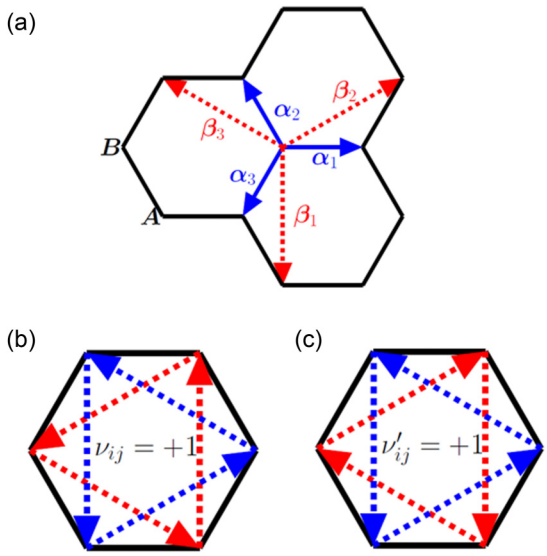

FIG. 1. (a) Honeycomb lattice structure. (b) The directions along which $\nu_{ij} = +1$ has been shown; otherwise $\nu_{ij} = -1$. (c) The directions along which $\nu'_{ij} = +1$ has been shown; otherwise $\nu'_{ij} = -1$.

respectively. Finally, $\nu'_{ij} = +\nu_{ij}$ for sublattice A and $\nu'_{ij} = -\nu_{ij}$ for sublattice B [Fig. 1(c)]. The zero-temperature ground state of the Hamiltonian [Eq. (1)] is ferromagnetic for $J > -\frac{3\sqrt{3}}{2}\sum_p |D + pD'|$, $p = \pm 1$ in the absence of magnetic field. The magnetic field B is introduced in a Zeeman coupling term to stabilize the ferromagnetic ground state at finite temperature. The energy scale is set by choosing $J = 1$—all other parameters in the Hamiltonian are in units of J.

III. RESULTS

A. Spinon picture

The Hamiltonian (1) has a ferromagnetic ground state. This can be described as the condensation of one of the spin species. At low temperatures ($T \ll J$), the only dynamics comes from magnon excitations that carry the opposite spin. However, at finite temperatures ($T \sim J$), both spin species contribute to the dynamics of the system. We start the discussion of our results with the general consideration of both spins contributing to the dynamics and later demonstrate that this naturally reduces to the magnon picture at low temperatures. We apply the Schwinger-boson mean field theory (SBMFT) to study the topological character of the magnetic system at finite temperatures. The Schwinger-boson representation consists of mapping the spin operators into spinons as $S_i^+ = c_{i,\uparrow}^\dagger c_{i,\downarrow}$, $S_i^- = c_{i,\downarrow}^\dagger c_{i,\uparrow}$, $S_i^z = \frac{1}{2}(c_{i,\uparrow}^\dagger c_{i,\uparrow} - c_{i,\downarrow}^\dagger c_{i,\downarrow})$, where $c_{i,s}$ and $c_{i,s}^\dagger$ are the annihilation and creation operators of spin-1/2 up ($s = +1$) or down ($s = -1$) spinons, respectively. The constraint $\sum_s c_{i,s}^\dagger c_{i,s} = 2S$, $\forall i$ on the bosonic operators ensures the fulfillment of the spin-S algebra.

After applying Schwinger-boson transformation along with the constraint, and using a mean field approximation to reduce the four-body operators to bilinear forms, the spin model Eq. (1) is mapped to the mean field Hamiltonian,

$$\begin{aligned}\mathcal{H} = &-\eta J \sum_{\langle i,j\rangle,s} [\hat{c}_{i,s}^\dagger \hat{c}_{j,s} + \text{H.c.}] + \sum_{i,s}\left(\lambda - \frac{sB}{2}\right)\hat{c}_{i,s}^\dagger \hat{c}_{i,s} \\ &+ \frac{D}{2}\sum_{\langle\langle ij\rangle\rangle,s} [(i\nu_{ij} s\zeta_{-s} + s\xi_{-s})\hat{c}_{i,s}^\dagger \hat{c}_{j,s} + \text{H.c.}] \\ &+ \frac{D'}{2}\sum_{\langle\langle ij\rangle\rangle,s} [(i\nu'_{ij} s\zeta_{-s} + s\xi'_{-s})\hat{c}_{i,s}^\dagger \hat{c}_{j,s} + \text{H.c.}], \end{aligned} \tag{2}$$

where the mean field parameters are defined as $\eta = \sum_s \langle \hat{\chi}_{ij,s}\rangle \equiv \sum_s \langle \hat{c}_{i,s}^\dagger \hat{c}_{j,s}\rangle$ evaluated on the nearest-neighbor bonds and $\zeta_s = \frac{1}{2}\langle \hat{\chi}_{ij,s} + \hat{\chi}_{ji,s}\rangle$, $\xi_s = \frac{\nu_{ij}}{2i}\langle \hat{\chi}_{ij,s} - \hat{\chi}_{ji,s}\rangle$, and $\xi'_s = \frac{\nu'_{ij}}{2i}\langle \hat{\chi}_{ij,s} - \hat{\chi}_{ji,s}\rangle$, evaluated on next-nearest-neighbor bonds. The terms associated with the parameters $\eta, \nu_{ij}\zeta_{-s}$ of spinon Hamiltonian Eq. (2) constitute the Kane-Mele-Haldane model [4]. The term with parameter $\nu'_{ij}\zeta_{-s}$ corresponds to the antichiral hopping term introduced in Ref. [12]. The terms with the parameters ξ_s and ξ'_s have no effect on the energy or the topological character of the bands, as the parameters are found to be much smaller compared to other mean field parameters. λ is the Lagrange undetermined multiplier introduced to implement the local constraint. Fourier transformation of the mean field Hamiltonian in momentum space yields

$$\mathcal{H}_{sp}^{mf} = \sum_{\boldsymbol{k}\in \text{B.Z.},s} \Psi_{\boldsymbol{k},s}^\dagger [g_s(\boldsymbol{k})I + \boldsymbol{h}_s(\boldsymbol{k})\cdot\boldsymbol{\sigma}]\Psi_{\boldsymbol{k},s} + E_0, \tag{3}$$

where $\Psi_{\boldsymbol{k},s}^\dagger = (\hat{a}_{\boldsymbol{k},s}^\dagger, \hat{b}_{\boldsymbol{k},s}^\dagger)$. $\hat{a}_{\boldsymbol{k},s}^\dagger$ and $\hat{b}_{\boldsymbol{k},s}^\dagger$ are the creation operators for Schwinger bosons on sublattice A and sublattice B [see Fig. 1(a) of main text], respectively. $\boldsymbol{\sigma}_\alpha$ ($\alpha = x, y, z$) represents the Pauli matrices. The other terms are given by

$$\begin{aligned} g_s(\boldsymbol{k}) &= -\frac{sB}{2} + \lambda + sD\xi_{-s}\gamma_c^\beta + sD'\left(\xi'_{-s}\gamma_c^\beta - \zeta_{-s}\gamma_s^\beta\right), \\ h_s(\boldsymbol{k}) &= \begin{pmatrix} -J\eta\gamma_c^\alpha \\ J\eta\gamma_s^\alpha \\ -Ds\zeta_{-s}\gamma_s^\beta \end{pmatrix}, \\ E_0 &= 6N_u J\eta^2 - 6DN_u \sum_s s\zeta_s\xi_{-s} \\ &\quad - 6D'N_u \sum_s s\zeta_s\xi'_{-s} - 4SN_u\lambda + 3N_u JS^2, \end{aligned} \tag{4}$$

where $\gamma_c^\beta = \sum_j \cos(\boldsymbol{k}\cdot\boldsymbol{\beta}_j)$, $\gamma_s^\beta = \sum_j \sin(\boldsymbol{k}\cdot\boldsymbol{\beta}_j)$, $\gamma_c^\alpha = \sum_j \cos(\boldsymbol{k}\cdot\boldsymbol{\alpha}_j)$, $\gamma_s^\alpha = \sum_j \sin(\boldsymbol{k}\cdot\boldsymbol{\alpha}_j)$ and the vectors $\boldsymbol{\beta}_j$ and $\boldsymbol{\alpha}_j$ are shown in Fig. 1(a). N_u is the number of unit cells in the lattice. E_0 is the energy of the ground state and the energies of spinons are considered with respect to the ground state energy. The mean field parameters are obtained by solving a set of self-consistent equations, derived by minimizing the Helmholtz free energy at a particular temperature (Appendix A).

Band structure for spinons at a temperature $T = 0.25J$ is shown in Fig. 2(a). In the absence of DMI, the two bands cross linearly at the Dirac points **K** and **K′** [15]. A finite DMI opens up a gap with magnitude $\Delta_s = 3\sqrt{3}|D\zeta_{-s}|$ in each spinon sector at **K** and **K′** [4,16–19]. For the *anisotropic*

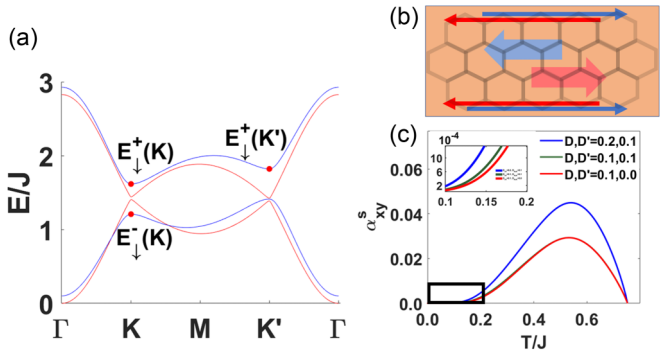

FIG. 2. (a) Band along symmetry lines ΓK, KM, MK', $K'\Gamma$ for $J = 1.0, B = 0.1, D_{ch} = 0.1, D_{Ach} = 0.05, T = 0.25$. The blue band is for down-spinon band and the red band is for up-spinon band. (b) The schematic of the antichiral contribution ($D = 0, D' \neq 0$) of the current from edge states (thin arrows) and bulk states (thick arrows). The colors red and blue are the contributions from the up-spinon and down-spinon, respectively. The direction of the thin arrows for each spinon sector are opposite and so there is a net spin current along the edges. Moreover, for each spinon sector the direction of the thick arrows and thin arrows are opposite, which in turn reduces the total spin-current flow along the edges. So, a net spin-current flow along the two edges are the evidence of antichiral state. (c) Nernst-conductivity vs temperature plot for different DMIs. The inset shows a magnified figure of the rectangular portion of the figure.

system ($D_A \neq D_B$) considered here, the gap opening is not symmetric and leads to a *tilting* of the spinon bands near the Dirac momenta. The band tilting for each band in each spinon sector, defined as the energy difference between two Dirac points in the same band, is given by $T_s^\tau = 3\sqrt{3}|D'\zeta_{-s}|$. While the antichiral DMI drives the tilting of the bands, it has no effect on the magnitude of the band gap. Crucially, the tilting is opposite for the two species of spinons. For the parameters chosen in Fig. 2(a), the gap and tilting for the up-spinon bands are smaller than those for the down-spinon bands. This is because in the presence of positive magnetic field $B = 0.1$ considered here, there are fewer down spinons and, consequently, $\zeta_\downarrow < \zeta_\uparrow$.

1. Nernst effect

The bands in each spinon sector carry nonzero Berry curvature, $\Omega_s^\tau(\mathbf{k})$, given by

$$\Omega_s^\tau(\mathbf{k}) = i \sum_{\tau' \neq \tau} \frac{\left\langle u_s^\tau(\mathbf{k}) \middle| \frac{\partial \mathcal{H}}{\partial k_x} \middle| u_s^{\tau'}(\mathbf{k}) \right\rangle \left\langle u_s^{\tau'}(\mathbf{k}) \middle| \frac{\partial \mathcal{H}}{\partial k_y} \middle| u_s^\tau(\mathbf{k}) \right\rangle}{\left[E_s^\tau(\mathbf{k}) - E_s^{\tau'}(\mathbf{k})\right]^2} - (k_x \leftrightarrow k_y), \tag{5}$$

where $\tau = +1(-1)$ represents upper(lower) band and $s = +1(-1)$ denotes the up-spinon(down-spinon) sector. $u_s^\tau(\mathbf{k})$ [$E_s^\tau(\mathbf{k})$] is the eigenvector (energy) of τth band at reciprocal space point $\mathbf{k}$ for spinon setor s. Detecting Berry curvature of spinon bands is more challenging than that for electrons. The absence of Pauli exclusion principle for the (bosonic) quasiparticles as well as their charge neutral character make the standard approaches used for electronic systems inapplicable. Spin Nernst effect has been proposed as a physical phenomenon to identify Berry curvature of spinon bands when there are comparable numbers of up and down spinons. Here we explore whether it can detect the existence of antichiral DMI. The Nernst conductivity has been calculated using the expression [4,20]

$$\alpha_{xy}^s = \frac{1}{2A} \sum_{\mathbf{k},s,\tau} s c_1\left[\rho_s^\tau(\mathbf{k})\right] \Omega_s^\tau(\mathbf{k}), \tag{6}$$

where A is the area of the system. Again, the Bose-Einstein distribution $\rho_s^\tau(\mathbf{k})$ and the function $c_1(x)$ are given by

$$\rho_s^\tau(\mathbf{k}) = \frac{1}{\left\{\exp\left[E_s^\tau(\mathbf{k})/T\right] - 1\right\}}, \qquad c_1(x) = (1+x)\ln(1+x) - x\ln x. \tag{7}$$

The results are plotted in Fig. 2(c) for some representative values of D and D'. Increase in D increases the band gap as well as the Berry curvature away from the Dirac points. As a result, the Nernst conductivity is substantially affected by D [Fig. 2(c)]. Conversely, since the Berry curvature is independent of D', the antichiral DMI has very little effect in the Nernst conductivity. The effect of D' on Nernst conductivity can be observed at low temperature due to tilting of the band structure [inset of Fig. 2(c)]. But, at higher temperature, the D' has no influence in Nernst conductivity, because the contributions from higher bands overshadow the effects of band tilting. So, the presence of D' in the system is very hard to detect using Nernst conductivity. Instead, we suggest an alternative way to detect the presence of antichiral DMI.

2. Spin current

The gapped bands are topologically nontrivial with Chern numbers $C_\uparrow^- = +1, C_\uparrow^+ = -1, C_\downarrow^- = -1, C_\downarrow^+ = +1$ [21]. Due to bulk-edge correspondence, we expect to observe edge states in a finite system. In the isotropic limit ($D' = 0$, i.e., $D_A = D_B$), the edge states are topologically protected by a chiral symmetry. The spinon currents along the two edges are equal and opposite for the up and down spinons. This results in a net flow of spins along the two edges in opposite directions—any scattering to the bulk states is prevented by symmetry constraints. For the asymmetric system considered here, D' induces an antichiral edge current of spinons where each species of spinon flows in the same direction along the two edges. This is balanced by the counterflow current of spinons in the opposite direction carried by the bulk modes. The antichiral DMI breaks the chiral symmetry protecting the edge states and enables scattering between edge and bulk states. This edge-to-bulk scattering produces the bulk current that balances the antichiral edge current. In the following we discuss how the bulk and edge state dispersion changes due to interplay between the chiral and antichiral DMI.

Figure 3 shows the spinon bands for a honeycomb nanoribbon with dimension 200×500 lattice sites with zigzag edges, together with the spin current profile along the width of the ribbon. Three different sets of (D, D') are chosen to illustrate the evolution of band dispersion and spin currents with changing DMI. For clarity of presentation, only one species of spinons is shown. Along with the total spin current, the contributions from the bulk and two edge modes are

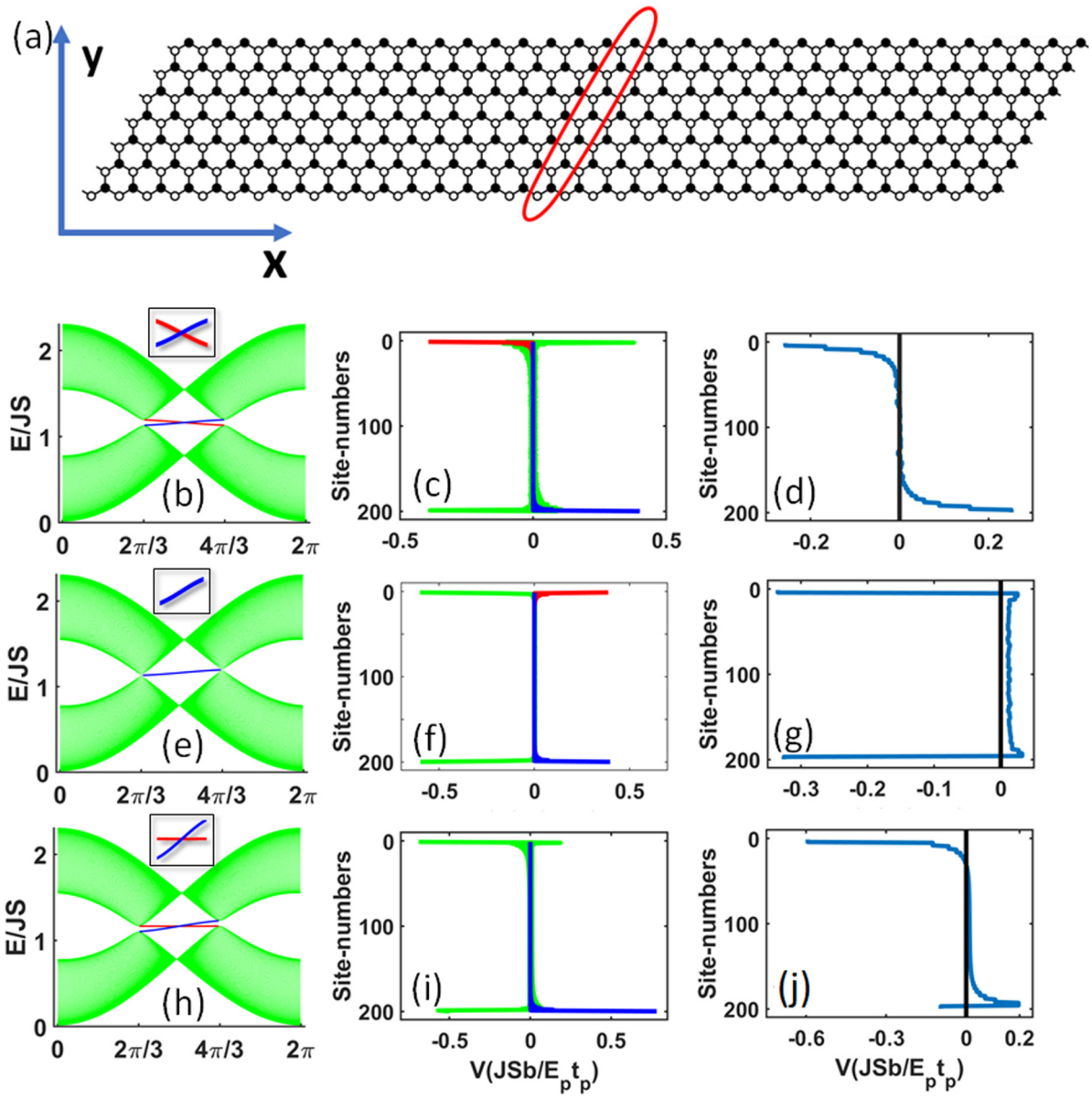

FIG. 3. (a) Honeycomb ribbon. The encircled sites are the basis of unit cell. The figure sets {(b) − (d)}, {(e) − (g)}, and {(h) − (j)} represent the result for down-spinon from 200 × 500 (width×length) stripe with DMIs $\{D = 0.1, D' = 0.001\}$, $\{D = 0.001, D' = 0.1\}$, and $\{D = 0.1, D' = 0.1\}$, respectively. The other parameters are $J = 1.0$, $B = 0.1$, $T = 0.5$ for all the plots. The figure sets {(b), (e), (h)} show the band structure and inset of the figures shows the magnified dispersion of the edge states. The figure sets {(c), (f), (i)} give the spatial current distribution along the width of the stripe, where b, E_p, and t_p are the lattice constant, Planck energy, and Planck time, respectively. The figure sets {(d), (g), (j)} show the average of spatial current distribution over four sites, respectively. In the figure sets {(b), (c), (e), (f), (h), (i)} the green, red, and blue plots correspond to bulk state, upper edge edge state, and lower-edge edge state, respectively. A nonzero net spin current along the edges in figures (g) and (j) are definitive signatures of antichiral edge states. The results for up-spinon are qualitatively the same, with the dispersion being opposite for the bulk and edge states relative to the down-spinons. Hence the up-spinons further contribute to the net spin current along the edges in the presence of antichiral edge states.

calculated separately to identify the effects of D' on each component. The spinon bands and the individual spin currents are color coded for easy identification. Green represents the bulk bands and their contribution to the spin current at each position along the width of the ribbon; red (blue) denotes the localized spinon mode and the associated spin current at the top (bottom) edge. A negative (positive) value of the spin current denotes spinon transport to the left (right) along the length of the ribbon.

For $D > D'$, the tilting of the bands is small and the dispersion of edge states at upper and lower edges are opposite, as shown in Fig. 3(b). The edge states are predominantly chiral in nature, and the spin current at the two edges are opposite in direction [Fig. 3(c), though not equal in magnitude since $D' \neq 0$ breaks chiral symmetry]. For large D' ($D' \gg D$), the tilting of the bands at the Dirac points is much greater and yields identical dispersion for the two edge states [Fig. 3(e)]. This results in *anti*-chiral edge states where the spin current

is in the same direction along both edges of the ribbon [Fig. 3(f)]. Finally, when $D \approx D'$, one of the edge states (the top edge in the present case) acquires a dispersionless character [Fig. 3(h)]. In other words, the edge state at the top is localized with no spinon transport, while the bottom edge has a finite dispersion with a finite edge current [Fig. 3(i)]. Because of $U(1)$ symmetry of each spinon sector, there is a counterpropagating bulk current to compensate the imbalance between edge states. The bulk current is not uniform across the width of the ribbon. Instead, it is primarily confined to a small region near the edges. At each edge, the bulk current opposes the edge current, with its magnitude decreasing rapidly away from the edges. To summarize, a nonzero net spin current along the two edges is a definitive signature of the existence of antichiral edge states. In principle, the anti-chiral edge states persist over the entire temperature range for which the short range correlations exist for the system ($k_BT \lesssim J$). However, at very high temperature the short range correlations η and ζ_s are very small (see Fig. 6 of Appendix A), which in turn makes the antichiral edge phenomenon experimentally undetectable at this limits. So we suggest the temperature range $k_BT \leqslant 0.6J$ is ideal for experimental detection of Antichiral edge modes.

B. Magnon picture

At low temperature one of the spinon species (say, the up-spinon) condenses at the lowest energy and forms the ferromagnetic ground state. The down-spinons are now excitations above the ground state. In contrast to the high temperature paramagnetic regime, at low temperatures only spin excitations above the ground state contribute to the dynamics of the system. Thus the system at low temperature can be described more simply using linearized Holstein-Primakoff bosons, which are given as

$$S_i^+ = \sqrt{2S}\hat{a}_i, \quad S_i^- = \sqrt{2S}\hat{a}_i^\dagger, \quad S_i^z = S - \hat{a}_i^\dagger\hat{a}_i, \tag{8}$$

where $\hat{a}_i$ is the annihilation operator of the Holstein-Primakoff boson. The real space Hamiltonian in terms of the Holstein-Primakoff boson is given by

$$\begin{aligned}\mathcal{H} = &-JS\sum_{\langle i,j\rangle}(\hat{a}_i^\dagger\hat{a}_j + \hat{a}_j^\dagger\hat{a}_i) - iDS\sum_{\langle\langle i,j\rangle\rangle}\nu_{ij}(\hat{a}_i^\dagger\hat{a}_j - \hat{a}_j^\dagger\hat{a}_i)\\ &- iD'S\sum_{\langle\langle i,j\rangle\rangle}\nu'_{ij}(\hat{a}_i^\dagger\hat{a}_j - \hat{a}_j^\dagger\hat{a}_i) + (B - 3JS)\sum_i \hat{a}_i^\dagger\hat{a}_i.\end{aligned} \tag{9}$$

In Fourier space the Hamiltonian is given by

$$\mathcal{H}_{sp}^{mf} = \sum_{\boldsymbol{k}\in \mathrm{BZ}} \Psi_{\boldsymbol{k}}^\dagger[g(\boldsymbol{k})I + \boldsymbol{h}(\boldsymbol{k})\cdot\boldsymbol{\sigma}]\Psi_{\boldsymbol{k}}, \tag{10}$$

where $\Psi_{\boldsymbol{k}}^\dagger = (\hat{a}_{\boldsymbol{k}}^\dagger, \hat{b}_{\boldsymbol{k}}^\dagger)$. $\hat{a}_{\boldsymbol{k}}^\dagger$ and $\hat{b}_{\boldsymbol{k}}^\dagger$ are the creation operators for the Holstein-Primakoff boson on sublattice A and sublattice B [see Fig. 1(a) of main text], respectively. $\boldsymbol{\sigma}_\alpha$ ($\alpha = x, y, z$) represents the Pauli matrices. The other terms are given by

$$g(\boldsymbol{k}) = B - 3JS + 2D'S\gamma_s^\beta, \quad h_s(\boldsymbol{k}) = \begin{pmatrix} -JS\gamma_c^\alpha \\ JS\gamma_s^\alpha \\ 2DS\gamma_s^\beta \end{pmatrix}, \tag{11}$$

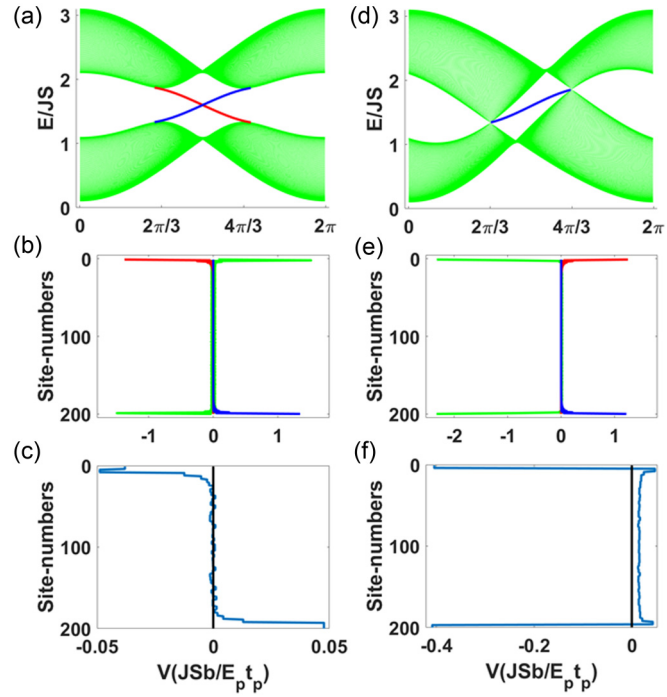

FIG. 4. Figure sets {(a) − (c)} and {(d) − (f)} represent the result for down-spinon from 200 × 500 (width×length) stripe with DMIs $\{D = 0.1, D' = 0.001\}$ and $\{D = 0.001, D' = 0.1\}$, respectively. The other parameters are $J = 1.0$, $B = 0.1$, $T = 0.5$ for all the plots. The figure sets {(a), (d)} show the magnon band structure of the stripe geometry. The figure sets {(b), (e)} give the spatial current distribution along the width of the stripe, where b, E_p, and t_p are the lattice constant, Planck energy, and Planck time, respectively. The figure sets {(c), (f)} show the average of spatial current distribution over four sites, respectively. In all the figures the green, red, and blue plots correspond to bulk state, upper-edge edge state, and lower-edge edge state, respectively. A nonzero net magnon current along the edges in figure (f) denotes the existence of antichiral edge states.

where $\gamma_c^\beta = \sum_j \cos(\boldsymbol{k}\cdot\boldsymbol{\beta}_j)$, $\gamma_s^\beta = \sum_j \sin(\boldsymbol{k}\cdot\boldsymbol{\beta}_j)$, $\gamma_c^\alpha = \sum_j \cos(\boldsymbol{k}\cdot\boldsymbol{\alpha}_j)$, $\gamma_s^\alpha = \sum_j \sin(\boldsymbol{k}\cdot\boldsymbol{\alpha}_j)$, and the vectors $\boldsymbol{\beta}_j$ and $\boldsymbol{\alpha}_j$ are shown in Fig. 1(a). The magnon Hamiltonian is identical to the down-spinon Hamiltonian at low temperatures, as the mean field parameters of the spinon Hamiltonian reduce to the following values: $\eta = S$, $\zeta_\uparrow = 2S$, $\zeta_\downarrow = \xi_s = \xi_s' = 0$ (see Fig. 6) and the Lagrange's undetermined multiplier becomes $\lambda = 3JS + B/2$. In other words, the spinon Hamiltonian naturally converges to the magnon Hamiltonian at low T. Figure 4 shows the results obtained using the magnon picture. The results agree well with those for the down spinon sector in the spinon picture.

C. Experimental detection

How does one detect antichiral spin currents experimentally? We suggest a suite of experimental probes that, taken together, can provide a "smoking-gun" signature of the existence of antichiral edge states. First, magnetic force microscopy (MFM) offers a promising experimental technique to measure the spinon current across the nanoribbon and hence can detect the presence of antichiral edge states. A

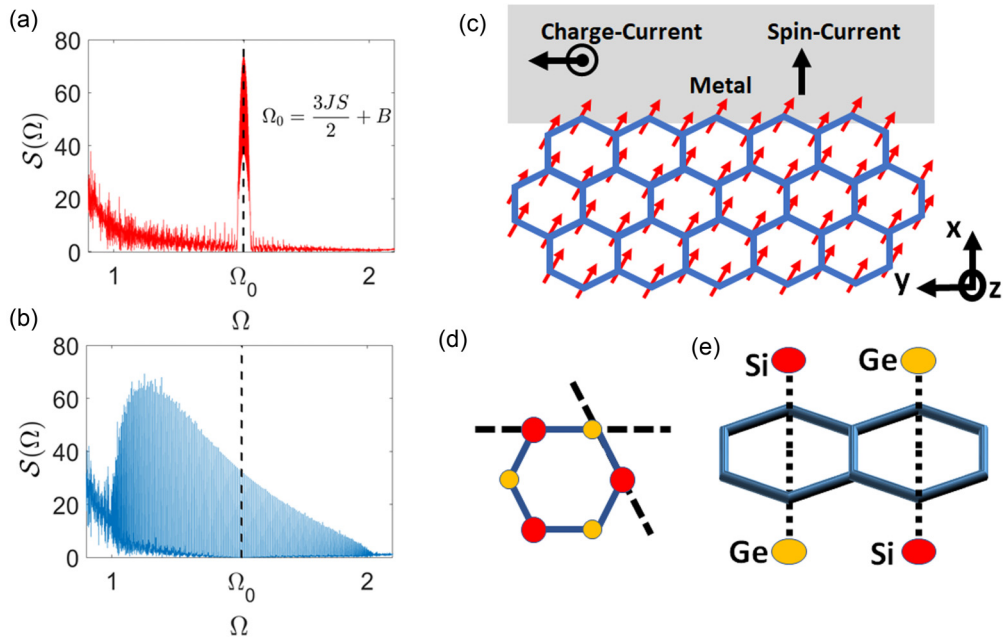

FIG. 5. (a),(b) Dynamical spin structure factor for two edges at temperature $T = 0.4J$, with parameters $D = 0.1, D' = 0.09, B = 0.01$. Red and blue colors denote upper and lower edges. (c) The experimental setup for spin Hall noise spectroscopy. (d) A ferromagnetic material with two different sublatices with a mirror symmetric plane along the dashed lines. (e) A proposed material based on real materials $CrGeTe_3$ and $CrSiTe_3$ to realize antichiral edge states.

nonzero value of net spin current along the two edges provides a direct evidence of antichiral edge states. Current MFM techniques can probe the local spin current in a finite sample to a resolution of a few nm. Since the topological character of the spinon bands for the different ranges of anisotropic DMI is reflected in distinct current profile across the ribbon, we believe MFM provides a promising experimental technique to identify antichiral edge states in real quasi-2D materials. Second, inelastic neutron scattering spectra can indirectly detect the presence of antichiral edge modes by probing the magnon band structure. If the bands are tilted or the energy at K and K' point is unequal, it will suggest the presence of antichiral edge modes.

Finally, we show that probing the low energy excitation spectrum offers a powerful probe to detect the asymmetry of the two edges in the limit of $D = D'$, when one of the edge states acquires a dispersionless character compared to the other edge. This low energy spectrum is readily obtained from calculating the dynamical-spin structure factor (DSSF). The DSSF at the edge of a finite system is (Appendix C) defined as $\mathcal{S}(\Omega) = i \sum_{l\in\text{edge}} [\mathcal{S}^{xx}_{ll}(\Omega) + \mathcal{S}^{zz}_{ll}(\Omega)]$, where $\mathcal{S}^{\alpha\alpha}_{ij}(\Omega) = -i \int_{-\infty}^{\infty} dt\, e^{-i\Omega t} \langle \hat{S}^{\alpha}_i(t) \hat{S}^{\alpha}_j(0) \rangle_0$. This offers a promising route to detecting antichiral edge states. The DSSF, shown in Figs. 5(a) and 5(b) for different edges, can be interpreted as the number of edge magnons present in a given energy level, and is proportional to the product of the density of states and Bose-Einstein distribution for the corresponding energy level. The signature of the edge states is reflected in the features of the DSSF near $\Omega = \frac{3J}{2} + B$, which is the energy of the edge states in the absence of any DMI. Our results show that $\mathcal{S}(\Omega)$ is dramatically different for the two edges for strong antichiral edge states, viz., when $|D| \approx |D'|$ (equivalently $D_A \gg D_B$ or $D_B \gg D_A$). The DSSF can be measured using the experimental setup shown in Fig. 5(c), according to Ref. [22]. The quantum fluctuation of the spins at the edges gives rise to spin current in metal and as a consequence the spin current gives rise to the charge current in transverse direction due to inverse spin Hall effect. Measurement of the noise spectrum in the charge current gives the information of the DSSF.

D. Material realization

The presence of antichiral DMI requires two in-equivalent sublattices in the 2D-honeycomb lattice, as shown in Fig. 5(d). The presence of two different types of atoms will result in asymmetric DMI, leading to a broken inversion symmetry and nonzero D'. Mirror symmetry along the dotted lines prevents any nonzero perpendicular DMI on nearest-neighbor bonds, whereas in-plane mirror symmetry suppresses any in-plane DMI. While we are not aware of any such material at present, the recent discovery of ferromagnetic order in the 2D limit of several Cr-based compounds including CrI_3 [2], $CrBr_3$ [23–25], $CrSrTe_3$ [25], and $CrGeTe_3$ [26] as well as the Fe-based family of compounds $AFe_2(PO_4)_2$ (A=Ba, Cs, K, La) [3] offer great promise. These quasi-2D materials consist of weakly van der Waals–coupled honeycomb ferromagets. The presence of chiral DMI in some members of this family [2] has been established using inelastic neutron scattering spectroscopy. In materials like $CrSrTe_3$ and $CrGeTe_3$, the presence of inversion center at the center of honeycomb cell makes the two sublattices equivalent. The inversion symmetry can be removed by replacing every other Ge atom by an Si atom as depicted in Fig. 5(e). In a similar vein, replacement of P atom by another group V element in $AFe_2(PO_4)_2$ (A=Ba, Cs, K, La) [3] will break the inversion symmetry of the lattice. The breaking of inversion symmetry may, in principle, give rise to additional interactions in these materials,

e.g., nearest-neighbor DMI. However, we have verified that inclusion of additional interactions, including nearest-neighbor DMI as well as second and third nearest-neighbor Heisenberg interactions only modifies the linear dispersion of the edge states and does not suppress the appearance of antichiral edge states (Appendix D).

IV. CONCLUSION

In conclusion, we have studied a Heisenberg ferromagnet with additional next-nearest-neighbor DMIs on a honeycomb lattice with broken sublattice symmetry. The unequal DMI between atoms on different sublattices, together with the broken chiral symmetry, results in the emergence of antichiral edge states, in addition to the normal chiral modes. This is manifested in unique spin current distribution across the width of a finite system with ribbon geometry. Interestingly, a uncompensated antichiral edge current exists, when antichiral DM interaction D' is larger than the chiral DM interaction D at a temperature compared to the ferromagnetic Heisenberg interaction J (i.e., $k_BT \approx J$). We have shown that the antichiral edges states result in a number of observable physical signatures, including a nonzero net spin current along the edges (that is only compensated by counterflowing bulk spin current) and strong anisotropy in the dynamic spin structure factor at the opposite edges. These unique features serve as smoking-gun signatures for the existence of antichiral edge states. We propose experimental probes to detect the presence of antichiral edge states via these features as well as a potential material where such states may be realized experimentally. In this work, the stability of the ferromagnetism in the proposed material is not studied. So, in future, further studies need to be done to identify the presence of ferromagnetism and antichiral DM interaction in the proposed materials.

ACKNOWLEDGMENTS

Financial support from the Ministry of Education, Singapore, in the form of Grant No. MOE2018-T1-1-021 is gratefully acknowledged.

APPENDIX A: SCHWINGER BOSON MEAN FIELD THEORY

The spin Hamiltonian is

$$\mathcal{H} = -J\sum_{\langle i,j\rangle} \boldsymbol{S}_i\cdot\boldsymbol{S}_j + D\sum_{\langle\langle i,j\rangle\rangle} \nu_{ij}\hat{z}\cdot(\boldsymbol{S}_i\times\boldsymbol{S}_j) + D'\sum_{\langle\langle i,j\rangle\rangle}\nu'_{ij}\hat{z}\cdot(\boldsymbol{S}_i\times\boldsymbol{S}_j) - B\sum_i S_i^z. \tag{A1}$$

After using the Schwinger-boson transformation and the constraints, the spinon Hamiltonian reads as

$$\begin{aligned}\mathcal{H}_{sp} = &-\frac{J}{2}\sum_{\langle i,j\rangle}(\hat{c}^\dagger_{i,\uparrow}\hat{c}^\dagger_{j,\downarrow}\hat{c}_{i,\downarrow}\hat{c}_{j,\uparrow} + \hat{c}^\dagger_{i,\downarrow}\hat{c}^\dagger_{j,\uparrow}\hat{c}_{i,\uparrow}\hat{c}_{j,\downarrow}) - \frac{J}{4}\sum_{\langle i,j\rangle}(\hat{c}^\dagger_{i,\uparrow}\hat{c}_{i,\uparrow}\hat{c}^\dagger_{j,\uparrow}\hat{c}_{j,\uparrow} + \hat{c}^\dagger_{i,\downarrow}\hat{c}_{i,\downarrow}\hat{c}^\dagger_{j,\downarrow}\hat{c}_{j,\downarrow} + \hat{c}^\dagger_{i,\uparrow}\hat{c}_{i,\uparrow}\hat{c}^\dagger_{j,\uparrow}\hat{c}_{j,\uparrow} + \hat{c}^\dagger_{i,\downarrow}\hat{c}_{i,\downarrow}\hat{c}^\dagger_{j,\downarrow}\hat{c}_{j,\downarrow})\\
&+\frac{iD}{2}\sum_{\langle\langle i,j\rangle\rangle}\nu_{ij}(\hat{c}^\dagger_{i,\uparrow}\hat{c}_{i,\downarrow}\hat{c}^\dagger_{j,\downarrow}\hat{c}_{j,\uparrow} - \hat{c}^\dagger_{i,\downarrow}\hat{c}_{i,\uparrow}\hat{c}^\dagger_{j,\uparrow}\hat{c}_{j,\downarrow}) + \frac{iD'}{2}\sum_{\langle\langle i,j\rangle\rangle}\nu'_{ij}(\hat{c}^\dagger_{i,\uparrow}\hat{c}_{i,\downarrow}\hat{c}^\dagger_{j,\downarrow}\hat{c}_{j,\uparrow} - \hat{c}^\dagger_{i,\downarrow}\hat{c}_{i,\uparrow}\hat{c}^\dagger_{j,\uparrow}\hat{c}_{j,\downarrow})\\
&-\frac{B}{2}\sum_i(\hat{c}^\dagger_{i,\uparrow}\hat{c}_{i,\uparrow} - \hat{c}^\dagger_{i,\downarrow}\hat{c}_{i,\downarrow}) + \sum_i\lambda_i(\hat{c}^\dagger_{i,\uparrow}\hat{c}_{i,\uparrow} + \hat{c}^\dagger_{i,\downarrow}\hat{c}_{i,\downarrow} - 2S) + 3N_uJS^2 - 4SN_u\lambda.\end{aligned} \tag{A2}$$

The bond operators have to be chosen such that the total number of spinon is conserved in the mean field Hamiltonian which is equivalent to S_z conservation in terms of spin [27]. Defining the bond operators, $\hat{\chi}_{ij} = \hat{c}^\dagger_{i,s}\hat{c}_{j,s}$ and $\hat{\chi}_{ij} = (\hat{\chi}_{ij,\uparrow} + \hat{\chi}_{ij,\downarrow})/2$, we can rewrite the Hamiltonian as

$$\begin{aligned}\mathcal{H}_{sp} = &-2J\sum_{\langle i,j\rangle} :\hat{\chi}^\dagger_{ij}\hat{\chi}_{ij}: - \frac{D}{2}\sum_{\langle\langle i,j\rangle\rangle} i\nu_{ij}(:\hat{\chi}^\dagger_{ij,\uparrow}\hat{\chi}_{ij,\downarrow}: - :\hat{\chi}^\dagger_{ij,\downarrow}\hat{\chi}_{ij,\uparrow}:) - \frac{D'}{2}\sum_{\langle\langle i,j\rangle\rangle} i\nu'_{ij}(:\hat{\chi}^\dagger_{ij,\uparrow}\hat{\chi}_{ij,\downarrow}: - :\hat{\chi}^\dagger_{ij,\downarrow}\hat{\chi}_{ij,\uparrow}:)\\
&-\frac{B}{2}\sum_i(\hat{c}^\dagger_{i,\uparrow}\hat{c}_{i,\uparrow} - \hat{c}^\dagger_{i,\downarrow}\hat{c}_{i,\downarrow}) + \lambda\sum_{is}\hat{c}^\dagger_{i,s}\hat{c}_{i,s} - 4SN_u\lambda + 3N_uJS^2.\end{aligned} \tag{A3}$$

New bond operators are defined so that corresponding mean field parameters are real: $\hat{A}_{ij,s} = \frac{1}{2}(\hat{\chi}_{ij,s} + \hat{\chi}_{ji,s})$, $\hat{B}_{ij,s} = \frac{\nu_{ij}}{2i}(\hat{\chi}_{ij,s} - \hat{\chi}_{ji,s})$, and $\hat{B'}_{ij,s} = \frac{\nu'_{ij}}{2i}(\hat{\chi}_{ij,s} - \hat{\chi}_{ji,s})$. Defining mean field parameters $\eta = \langle\hat{\chi}^\dagger_{ij}\rangle = \langle\hat{\chi}_{ij}\rangle$, $\zeta_s = \langle\hat{A}^\dagger_{ij,s}\rangle = \langle\hat{A}_{ij,s}\rangle$, $\xi_s = \langle\hat{B}^\dagger_{ij,s}\rangle = \langle\hat{B}_{ij,s}\rangle$, and $\xi'_s = \langle\hat{B'}^\dagger_{ij,s}\rangle = \langle\hat{B'}_{ij,s}\rangle$, the quartic terms of Hamiltonian can be decoupled into quadratic and the mean-field spinon Hamiltonian takes the form as

$$\begin{aligned}\mathcal{H}^{mf}_{sp} = &-\eta J\sum_{\langle i,j\rangle,s}[\hat{c}^\dagger_{i,s}\hat{c}_{j,s} + \text{H.c.}] + \frac{D}{2}\sum_{\langle\langle ij\rangle\rangle,s}\left[i\nu_{ij}s\zeta_{-s}\hat{c}^\dagger_{i,s}\hat{c}_{j,s} + \text{H.c.}\right] + \frac{D}{2}\sum_{\langle\langle ij\rangle\rangle,s}\left[s\xi_{-s}\hat{c}^\dagger_{i,s}\hat{c}_{j,s} + \text{H.c.}\right]\\
&+\frac{D'}{2}\sum_{\langle\langle ij\rangle\rangle,s}\left[i\nu'_{ij}s\zeta_{-s}\hat{c}^\dagger_{i,s}\hat{c}_{j,s} + \text{H.c.}\right] + \frac{D'}{2}\sum_{\langle\langle ij\rangle\rangle,s}\left[s\xi'_{-s}\hat{c}^\dagger_{i,s}\hat{c}_{j,s} + \text{H.c.}\right] + \sum_{i,s}\left(\lambda - \frac{sB}{2}\right)\hat{c}^\dagger_{i,s}\hat{c}_{i,s} + 6N_uJ\eta^2\\
&-6DN_u\sum_s s\zeta_s\xi_{-s} - 6D'N_u\sum_s s\zeta_s\xi'_{-s} - 4SN_u\lambda + 3N_uJS^2.\end{aligned} \tag{A4}$$

Fourier transformation of the mean field Hamiltonian to momentum space yields

$$\mathcal{H}_{sp}^{mf} = \sum_{\boldsymbol{k}\in \mathrm{BZ},s} \Psi_{\boldsymbol{k},s}^{\dagger}[g_s(\boldsymbol{k})I + \boldsymbol{h}_s(\boldsymbol{k})\cdot\boldsymbol{\sigma}]\Psi_{\boldsymbol{k},s} + E_0, \tag{A5}$$

where $\Psi_{\boldsymbol{k},s}^{\dagger} = (\hat{a}_{\boldsymbol{k},s}^{\dagger}, \hat{b}_{\boldsymbol{k},s}^{\dagger})$. $\hat{a}_{\boldsymbol{k},s}^{\dagger}$ and $\hat{b}_{\boldsymbol{k},s}^{\dagger}$ are the creation operators for Schwinger bosons on sublattice A and sublattice B [see Fig. 1(a) of main text], respectively. $\boldsymbol{\sigma}_{\alpha}(\alpha = x, y, z)$ represents the Pauli matrices. The other terms are given by

$$g_s(\boldsymbol{k}) = -\frac{sB}{2} + \lambda + sD\xi_{-s}\gamma_c^{\beta} + sD'\left(\xi'_{-s}\gamma_c^{\beta} - \zeta_{-s}\gamma_s^{\beta}\right),$$

$$h_s(\boldsymbol{k}) = \begin{pmatrix} -J\eta\gamma_c^{\alpha} \\ J\eta\gamma_s^{\alpha} \\ -Ds\zeta_{-s}\gamma_s^{\beta} \end{pmatrix},$$

$$E_0 = 6N_uJ\eta^2 - 6DN_u\sum_s s\zeta_s\xi_{-s} - 6D'N_u\sum_s s\zeta_s\xi'_{-s} - 4SN_u\lambda + 3N_uJS^2, \tag{A6}$$

where $\gamma_c^{\beta} = \sum_j \cos(\boldsymbol{k}\cdot\boldsymbol{\beta}_j)$, $\gamma_s^{\beta} = \sum_j \sin(\boldsymbol{k}\cdot\boldsymbol{\beta}_j)$, $\gamma_c^{\alpha} = \sum_j \cos(\boldsymbol{k}\cdot\boldsymbol{\alpha}_j)$, $\gamma_s^{\alpha} = \sum_j \sin(\boldsymbol{k}\cdot\boldsymbol{\alpha}_j)$, and the vectors $\boldsymbol{\beta}_j$ and $\boldsymbol{\alpha}_j$ are shown in Fig. 1(a). N_u is the number of unit cells in lattice. E_0 is the energy of the ground state and the energies of spinons are considered with respect to the ground state energy.

After diagonalizing the k-space Hamiltonian we get

$$\mathcal{H}_{sp}^{mf} = E_0 + \sum_{\boldsymbol{k},s,\tau} E_s^{\tau}(\boldsymbol{k})\hat{c}_{\boldsymbol{k},\tau,s}^{\dagger}\hat{c}_{\boldsymbol{k},\tau,s}, \tag{A7}$$

where the relative energies,

$$E_s^{\tau}(\boldsymbol{k}) = g_s(\boldsymbol{k}) + \tau|h_s(\boldsymbol{k})|, \tag{A8}$$

refer to the upper ($\tau = +1$) and the lower ($\tau = -1$) band for each spinon sector $s = \pm 1$.

From this we get the internal energy and the entropy of the noninteracting system as

$$U = E_0 + \sum_{\boldsymbol{k},s,\tau} \rho_s^{\tau}(\boldsymbol{k})E_s^{\tau}(\boldsymbol{k}),$$

$$S = k_B\sum_{\boldsymbol{k},s,\tau}\left\{\left[1+\rho_s^{\tau}(\boldsymbol{k})\right]\ln\left[1+\rho_s^{\tau}(\boldsymbol{k})\right] - \rho_s^{\tau}(\boldsymbol{k})\ln\rho_s^{\tau}(\boldsymbol{k})\right\}, \tag{A9}$$

where $\rho_s^{\tau}(\boldsymbol{k}) = \{\exp[E_s^{\tau}(\boldsymbol{k})] - 1\}^{-1}$ is the Bose-Einstein distribution of spin-s spinons in the τ band. The Helmholtz free energy is given by

$$G = U - TS = E_0 - k_BT\sum_{\boldsymbol{k},s,\tau}\ln\left(\frac{1}{1-\exp\left(\frac{-E_s^{\tau}(\boldsymbol{k})}{k_BT}\right)}\right). \tag{A10}$$

After minimizing the Helmholtz free energy with respect to the mean field parameters, we get six self consistent equations, given by

$$2S = \frac{1}{2N_u}\sum_{\boldsymbol{k},\tau,s}\rho_s^{\tau}(\boldsymbol{k}),$$

$$1 = -\frac{J}{12N_u}\sum_{\boldsymbol{k},s,\tau}\tau\frac{\rho_s^{\tau}(\boldsymbol{k})}{|h_s|}\left|\sum_j e^{i\boldsymbol{k}\cdot\boldsymbol{\alpha}_j}\right|^2,$$

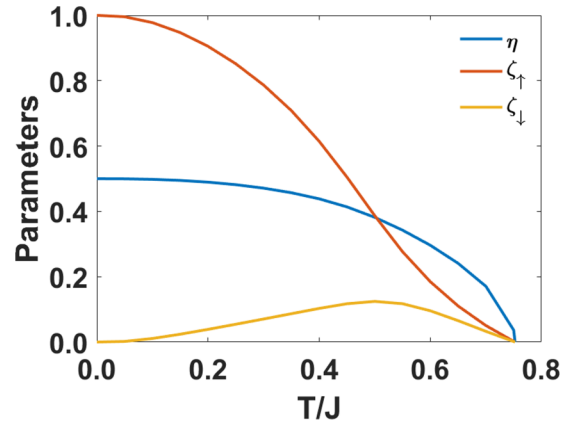

FIG. 6. Plot of mean-field parameters, for $J = 1.0, D = 0.1, D' = 0.05, B = 0.1$.

$$D\xi_s + D'\xi'_s = \frac{1}{6N_u}\sum_{\boldsymbol{k},\tau}\left(D' - \tau s\frac{D^2\zeta_{-s}\gamma_s^{\beta}}{|h_s|}\right)\rho_s^{\tau}(\boldsymbol{k})\gamma_s^{\beta},$$

$$\zeta_s = \frac{1}{6N_u}\sum_{\boldsymbol{k},\tau}\rho_s^{\tau}(\boldsymbol{k})\sum_j\cos(\boldsymbol{k}\cdot\boldsymbol{\beta}_j). \tag{A11}$$

The mean field parameters are obtained by solving these six self-consistent equations. It is notable that the mean field parameter η can be chosen as real, absorbing the complex phase factor into operator $\hat{c}_{i,s}$. Similarly, all the mean field parameters can be chosen to be real valued. Using the parameters, we plot the band structure and evaluate corresponding topological information. For a fixed set of J, D, D', B, the mean field parameters are solved and plotted against temperature T in Fig. 6. The parameters η and ζ_s represent short range correlations identifying magnetic ordering and serve as order parameters for the transition from paramagnet with short-range correlations to completely uncorrelated paramagnet at higher temperatures [28]. The constraint λ is considered uniform throughout the lattice to retain the translational symmetry of the lattice.

At low temperatures, finite, nonzero values of η and $\zeta_{\uparrow}$ denote ferromagnetic ordering. A positive B determines that the spins are all aligned along the $+ve$ z direction at $T = 0$. In other words, the system is populated with up-spinons. As the temperature increases, thermally excited down-spinons are generated, resulting in a finite, nonzero $\zeta_{\downarrow}$. Finally, at high temperatures, a vanishing of all the mean field parameters denotes a transition from paramagnetic phase with finite short range correlations to a totally uncorrelated paramagnetic phase. The paramagnetic phase transition with all zero correlations is expected to be an outcome of large-N expansion. It has been shown for the Heisenberg model that taking into account the quantum fluctuations in the mean field parameter removes the phase transition [29].

APPENDIX B: CALCULATION OF THE EDGE-STATE AND VELOCITY DISTRIBUTION ON A STRIPE GEOMETRY

The Hamiltonian in the tight binding Hamiltonian can be written as

$$\mathcal{H} = \sum_{ij} t_{ij}|i\rangle\langle j|, \tag{B1}$$

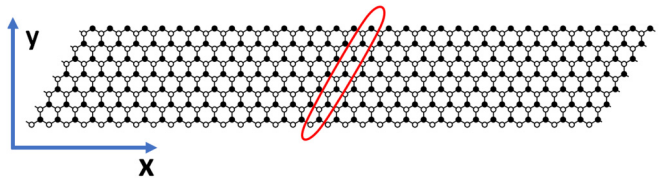

FIG. 7. Honeycomb lattice structure of size (20 × 14) with periodic boundary condition along x axis and open boundary condition along y axis. The encircled sites are the basis of the unit cell.

where i and j are the sites of lattice and t_{ij} is the hopping amplitude. More explicitly the Hamiltonian can be written as a matrix form as [30]

$$\mathcal{H} = \sum_{m,s} [\Psi^\dagger_{m,s} U_s \Psi_{m,s} + \Psi^\dagger_{m,s} T_s \Psi_{m+1,s} + \Psi^\dagger_{m+1,s} T_s^\dagger \Psi_{m,s}], \tag{B2}$$

where $\Psi^\dagger_{m,s} = (\hat{b}^\dagger_{1,m,s}, \hat{a}^\dagger_{2,m,s}, \ldots, \hat{a}^\dagger_{N_i,m,s})$ and N_i is the number of sites along the stripe (the sites inside the red circle of Fig. 7 make one stripe) and m denotes the stripe index and s denotes up- or down-spinon type. U_s and T_s are $N_i \times N_i$ matrices. Matrix U_s contains all the on-site and intrastripe hopping elements (inside the red circle of Fig. 7) and matrix T_s contains all the interstripe hopping elements.

Imposing a periodic boundary condition along the longitudinal direction as shown in Fig. 7, one can Fourier transform the Hamiltonian with a 1D Bloch-wave vector, given by $\Psi_{m,s} = (1/\sqrt{M}) \sum_{k=0}^{M-1} \Psi_{k,s} e^{-i2\pi km/M}$, where M is the number of stripes along the x axis in Fig. 7. After Fourier transform the Hamiltonian can be written as

$$H = \sum_k \Psi^\dagger_k \left[U_s + \left(T_s e^{i\frac{2k\pi}{M}} + \text{H.c.}\right)\right] \Psi_{k,s} = \sum_k \Psi^\dagger_k H_{k,s} \Psi_{k,s}. \tag{B3}$$

The Hamiltonian can be diagonalized as

$$\epsilon_{k,s} = P^\dagger H_{k,s} P, \tag{B4}$$

where P is a unitary matrix and the corresponding eigenvector is given by

$$\Psi^d_{k,s} = P^\dagger \Psi_{k,s}. \tag{B5}$$

Diagonalizing the momentum space Hamiltonian, we obtain the bands for the stripe geometry, as shown in Figs. 3(b), 3(e) and 3(h) of the main text.

The velocity operator, used to evaluate the spinon transport properties, are expressed in terms of the k-space eigenstates as [31,32]

$$\hat{v} = \sum_{ij} v_{ij} |i\rangle\langle j|, \tag{B6}$$

where the coefficient v_{ij} is given by

$$v_{ij} = \langle i|\hat{v}|j\rangle = -\frac{i}{\hbar}\langle i|[\hat{r}, \mathcal{H}]|j\rangle = -\frac{i}{\hbar}(\boldsymbol{r}_i - \boldsymbol{r}_j) t_{ij}. \tag{B7}$$

We have calculated the distribution of the velocity component along the x axis across the cross section of the ribbon, which is shown in Figs. 3(c), 3(f) and 3(i) of the main text.

APPENDIX C: CALCULATION OF THE DYNAMICAL SPIN STRUCTURE FACTOR

To calculate the dynamical spin structure factor, we have used the Holstein-Primakoff transformation as in Eq. (10). For the case of a ferromagnet with up spin at each site, the Holstein-Primakoff boson represents the down-spinons in the Schwinger-boson picture at low temperature. For simplicity, we calculate dynamical spin structure factor using Holstein-Primakoff bosons. However the lattice geometry and the diagonalization procedure are same as in Appendix B. For the site 1 of mth stripe (see Appendix B),

$$\begin{aligned}\hat{b}_{1,m}(t) &= \frac{1}{\sqrt{M}} \sum_{k=0}^{M-1} \hat{b}_{1,k}(t) e^{-i\frac{2\pi km}{M}} \\ &= \frac{1}{\sqrt{M}} \sum_{k=0}^{M-1} \sum_n P_{1,n} \hat{b}^d_{n,k}(t) e^{-i\frac{2\pi km}{M}},\end{aligned} \tag{C1}$$

where P is the unitary matrix for diagonalization and $\hat{b}^d_{n,k}$ is the bosonic operator after diagonalization and n denotes the band-index. The Hamiltonian can be written as

$$H_k = \sum_n \epsilon_n(k) \hat{b}^{d\dagger}_{n,k} \hat{b}^d_{n,k}. \tag{C2}$$

Using the above relation and Heisenberg's equation of motion it can be proved that

$$\begin{aligned}\hat{b}^{d\dagger}_{n,k}(t) &= \hat{b}^{d\dagger}_{n,k}(0) e^{i\epsilon_n(k)t}, \\ \hat{b}^d_{n,k}(t) &= \hat{b}^d_{n,k}(0) e^{-i\epsilon_n(k)t}.\end{aligned} \tag{C3}$$

The dynamical spin structure factor is given by

$$\begin{aligned}\mathcal{S}(\Omega) &= \sum_{m\in\text{edge}} \left[\mathcal{S}^{xx}_{mm}(\Omega) + \mathcal{S}^{zz}_{mm}(\Omega)\right] \\ &= \sum_{m\in\text{edge}} \left[\int_{-\infty}^{\infty} dt\, e^{-i\Omega t} \left(-i\langle \hat{S}^x_{1,m}(t) \hat{S}^x_{1,m}(0)\rangle\right)\right. \\ &\quad \left. + \int_{-\infty}^{\infty} dt\, e^{-i\Omega t} \left(-i\langle \hat{S}^z_{1,m}(t) \hat{S}^z_{1,m}(0)\rangle\right)\right] \\ &= -i \sum_m \int_{-\infty}^{\infty} dt\, e^{-i\Omega t} \left[\frac{S}{2} \langle \hat{b}_{1,m}(t) \hat{b}_{1,m}(0)\right. \\ &\quad + \hat{b}_{1,m}(t) \hat{b}^\dagger_{1,m}(0) + \hat{b}^\dagger_{1,m}(t) \hat{b}_{1,m}(0) + \hat{b}^\dagger_{1,m}(t) \hat{b}_{1,m}(0)\rangle \\ &\quad \left. + \langle S^2 - S\hat{b}^\dagger_{1,m}(0) \hat{b}_{1,m}(0) - S\hat{b}^\dagger_{1,m}(t) \hat{b}_{1,m}(t)\rangle\right] \\ &\quad \text{[Using Holstein-Primakoff transformation and} \\ &\quad \text{neglecting the higher order terms].}\end{aligned} \tag{C4}$$

Using Eq. (C1) and Eq. (C3), we get

$$\begin{aligned}\langle \hat{b}^{\dagger}_{1,m}(t)\hat{b}_{1,m}(0)\rangle &= \left\langle \frac{1}{\sqrt{M}}\sum_{k=0}^{M-1}\sum_{n} P^{*}_{1,n}\hat{b}^{d\dagger}_{n,k}(t)e^{i\frac{2\pi km}{M}} \right. \\ &\quad \left. \times \frac{1}{\sqrt{M}}\sum_{k'=0}^{M-1}\sum_{n'} P_{1,n'}\hat{b}^{d}_{n',k'}(0)e^{i\frac{2\pi k'm}{M}} \right\rangle \\ &= \frac{1}{M}\sum_{k=0}^{M-1}\sum_{n}\sum_{k'=0}^{M-1}\sum_{n'} P^{*}_{1,n}P_{1,n'}e^{i\epsilon_n(k)t} \\ &\quad \times \langle \hat{b}^{d\dagger}_{n,k}(0)\hat{b}^{d}_{n',k'}(0)\rangle \\ &= \frac{1}{M}\sum_{k=0}^{M-1}\sum_{n}|P_{1,n}|^2 e^{i\epsilon_n(k)t}n(\epsilon_n(k)), \end{aligned} \tag{C5}$$

where $n(\epsilon_n(k))$ is the Bose-Einstein distribution for energy $\epsilon_n(k)$.

Similarly,

$$\begin{aligned}\langle \hat{b}_{1,m}(t)\hat{b}^{\dagger}_{1,m}(0)\rangle &= \frac{1}{M}\sum_{k=0}^{M-1}\sum_{n}|P_{1,n}|^2 e^{-i\epsilon_n(k)t}n(\epsilon_n(k)), \\ \langle \hat{b}^{\dagger}_{1,m}(t)\hat{b}^{\dagger}_{1,m}(0)\rangle &= \langle \hat{b}_{1,m}(t)\hat{b}_{1,m}(0)\rangle = 0, \\ \langle \hat{b}^{\dagger}_{1,m}(t)\hat{b}_{1,m}(t)\rangle &= \frac{1}{M}\sum_{k=0}^{M-1}\sum_{n}|P_{1,n}|^2 n(\epsilon_n(k)), \\ \langle \hat{b}^{\dagger}_{1,m}(0)\hat{b}_{1,m}(0)\rangle &= \frac{1}{M}\sum_{k=0}^{M-1}\sum_{n}|P_{1,n}|^2 n(\epsilon_n(k)). \end{aligned} \tag{C6}$$

Using Eq. (C5) and Eq. (C6) in Eq. (C4), we get

$$\begin{aligned}\mathcal{S}(\Omega) = -i\pi(M-1)\Bigg[&\frac{S}{2}\sum_{k=0}^{M-1}\sum_{n}|P_{1,n}(k)|^2 n(\epsilon_n(k))\delta(\Omega+\epsilon_n(k)) \\ &+\frac{S}{2}\sum_{k=0}^{M-1}\sum_{n}|P_{1,n}(k)|^2 n(\epsilon_n(k))\delta(\Omega-\epsilon_n(k)) \\ &+\left\{MS^2 - 2S\sum_{k=0}^{M-1}\sum_{n}|P_{1,n}(k)|^2 n(\epsilon_n(k))\right\}\delta(\Omega)\Bigg]. \end{aligned} \tag{C7}$$

APPENDIX D: MODULATION OF EDGE STATE DISPERSION IN THE PRESENCE OF OTHER INTERACTIONS IN A HONEYCOMB FERROMAGNET

The spin model discussed in the main text is very ideal. For example, the long range Heisenberg interactions are neglected. Moreover, the criteria to get the antichiral DM term D' is to break the inversion symmetry at the center of each honeycomb plaquette. The breaking of such symmetry might raise the nearest-neighbor out of plane DM interactions and also in plane DM interactions. At low temperature, the in plane interactions can be neglected, which gives rise to three magnon interactions in terms of Holstein Primakoff bosons. But, at high temperature, where the spin system can be treated in terms of Schwinger bosons, the in plane DM interaction gives rise to the mixing of two spinon sectors, in the presence of which the quasiparticles are mixed eigenstates of spin-up and spin-down sectors. Neglecting any presence of in plane DM interaction at low temperature, we can rewrite a more general Hamiltonian of the material as

$$\begin{aligned}\mathcal{H} = &J_1\sum_{\langle i,j\rangle}\boldsymbol{S}_i\cdot\boldsymbol{S}_j + J_2\sum_{\langle\langle i,j\rangle\rangle}\boldsymbol{S}_i\cdot\boldsymbol{S}_j + J_3\sum_{\langle\langle\langle i,j\rangle\rangle\rangle}\boldsymbol{S}_i\cdot\boldsymbol{S}_j + D_1\sum_{\langle ij\rangle_A}\nu_{ij}\hat{z}\cdot(\boldsymbol{S}_i\times\boldsymbol{S}_j) + D_2\sum_{\langle ij\rangle_B}\nu_{ij}\hat{z}\cdot(\boldsymbol{S}_i\times\boldsymbol{S}_j) \\ &+ D\sum_{\langle\langle ij\rangle\rangle_B}\nu_{ij}\hat{z}\cdot(\boldsymbol{S}_i\times\boldsymbol{S}_j) + D'\sum_{\langle\langle ij\rangle\rangle_B}\nu'_{ij}\hat{z}\cdot(\boldsymbol{S}_i\times\boldsymbol{S}_j) + B\sum_i \boldsymbol{S}_i, \end{aligned} \tag{D1}$$

where, the DM interactions D_1 and D_2 are defined on the nearest-neighbor bonds $\langle ij\rangle_A$ and $\langle ij\rangle_B$ as shown in Fig. 8.

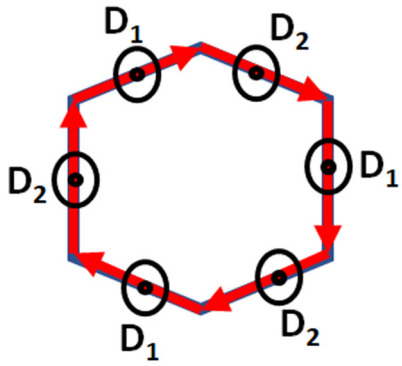

FIG. 8. DM interactions on nearest-neighbor bonds.

Furthermore, single ion anisotropy like terms act as a chemical potential for the spin excitation, which is taken into account in the magnetic field. To consider a more realistic situation, we have fixed the Heisenberg interactions present in the material CrI_3 [2], $J_1 = 2.09$ meV, $J_2 = 0.16$ meV, and $J_3 = 0.18$ meV. The nearest-neighbor DM terms and magnetic field are fixed as $D_1 = 0.1$ meV, $D_2 = 0.15$ meV, and $B = g\mu_B B_z = 0.01$ meV. We transformed the spin Hamiltonian into the magnon Hamiltonian using the Holstein Primakoff transformation defined in Eq. (10). Then, we plotted the band structure and dynamical spin structure factor in Fig. 9. It is noticeable that the qualitative behavior of the edge states is mostly dependent on the DM interactions D and D'. The presence of other interaction terms in the Hamiltonian just distorts the linear dispersion of the edge states.

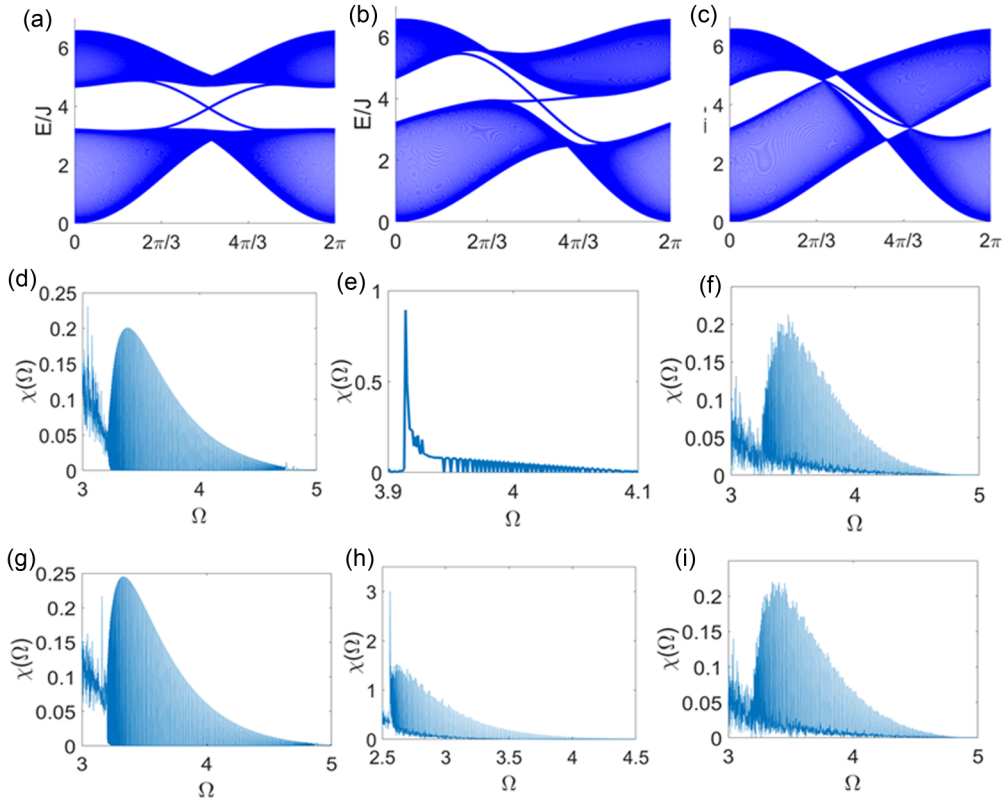

FIG. 9. Band structure of stripe geometry for parameters (a) $D = 0.31$ meV, $D' = 0.01$ meV, (b) $D = 0.31$ meV, $D' = 0.28$ meV, and (c) $D = 0.01$ meV, $D' = 0.31$ meV. The dynamical spin structure factor for upper edge at $T = 0.4$ for parameters (d) $D = 0.31$ meV, $D' = 0.01$ meV, (e) $D = 0.31$ meV, $D' = 0.28$ meV, and (f) $D = 0.01$ meV, $D' = 0.38$ meV. The dynamical spin structure factor for lower edge at $T = 0.4$ for parameters (g) $D = 0.31$ meV, $D' = 0.01$ meV, (h) $D = 0.31$ meV, $D' = 0.28$ meV, and (i) $D = 0.01$ meV, $D' = 0.38$ meV.

[1] F. D. M. Haldane, Phys. Rev. Lett. **61**, 1029 (1988).
[2] L. Chen, J.-H. Chung, B. Gao, T. Chen, M. B. Stone, A. I. Kolesnikov, Q. Huang, and P. Dai, Phys. Rev. X **8**, 041028 (2018).
[3] H.-S. Kim and H.-Y. Kee, npj Quantum Mater. **2**, 20 (2017).
[4] S. K. Kim, H. Ochoa, R. Zarzuela, and Y. Tserkovnyak, Phys. Rev. Lett. **117**, 227201 (2016).
[5] V. A. Zyuzin and A. A. Kovalev, Phys. Rev. Lett. **117**, 217203 (2016).
[6] R. Cheng, S. Okamoto, and D. Xiao, Phys. Rev. Lett. **117**, 217202 (2016).
[7] Y. Zhang, S. Okamoto, and D. Xiao, Phys. Rev. B **98**, 035424 (2018).
[8] Y. Onose, T. Ideue, H. Katsura, Y. Shiomi, N. Nagaosa, and Y. Tokura, Science **329**, 297 (2010).
[9] M. Hirschberger, J. W. Krizan, R. J. Cava, and N. P. Ong, Science **348**, 106 (2015).
[10] T. Ideue, Y. Onose, H. Katsura, Y. Shiomi, S. Ishiwata, N. Nagaosa, and Y. Tokura, Phys. Rev. B **85**, 134411 (2012).
[11] R. Hentrich, M. Roslova, A. Isaeva, T. Doert, W. Brenig, B. Büchner, and C. Hess, Phys. Rev. B **99**, 085136 (2019).
[12] E. Colomés and M. Franz, Phys. Rev. Lett. **120**, 086603 (2018).
[13] S. Mandal, R. Ge, and T. C. H. Liew, Phys. Rev. B **99**, 115423 (2019).
[14] M. Vila, N. T. Hung, S. Roche, and R. Saito, Phys. Rev. B **99**, 161404(R) (2019).
[15] S. S. Pershoguba, S. Banerjee, J. C. Lashley, J. Park, H. Ågren, G. Aeppli, and A. V. Balatsky, Phys. Rev. X **8**, 011010 (2018).
[16] S. A. Owerre, J. Phys.: Condens. Matter **28**, 386001 (2016).
[17] S. A. Owerre, J. Appl. Phys. **120**, 043903 (2016).
[18] S. A. Owerre, J. Phys. Commun. **1**, 021002 (2017).
[19] P. A. Pantaleón, R. Carrillo-Bastos, and Y. Xian, J. Phys.: Condens. Matter **31**, 085802 (2019).
[20] A. A. Kovalev and V. Zyuzin, Phys. Rev. B **93**, 161106(R) (2016).
[21] E. Matsuoka, K. Hayashi, A. Ikeda, K. Tanaka, T. Takabatake, and M. Matsumura, J. Phys. Soc. Jpn. **74**, 1382 (2005).
[22] D. G. Joshi, A. P. Schnyder, and S. Takei, Phys. Rev. B **98**, 064401 (2018).
[23] E. J. Samuelsen, R. Silberglitt, G. Shirane, and J. P. Remeika, Phys. Rev. B **3**, 157 (1971).
[24] I. Tsubokawa, J. Phys. Soc. Jpn. **15**, 1664 (1960).
[25] T. J. Williams, A. A. Aczel, M. D. Lumsden, S. E. Nagler, M. B. Stone, J.-Q. Yan, and D. Mandrus, Phys. Rev. B **92**, 144404 (2015).
[26] C. Gong, L. Li, Z. Li, H. Ji, A. Stern, Y. Xia, T. Cao, W. Bao, C. Wang, Y. Wang, Z. Q. Qiu, R. J. Cava, S. G. Louie, J. Xia, and X. Zhang, Nature **546**, 265 (2017).

[27] H. Lee, J. H. Han, and P. A. Lee, Phys. Rev. B **91**, 125413 (2015).
[28] S. Sarker, C. Jayaprakash, H. R. Krishnamurthy, and M. Ma, Phys. Rev. B **40**, 5028 (1989).
[29] O. Tchernyshyov and S. Sondhi, Nucl. Phys. B **639**, 429 (2002).
[30] A. Guclu, P. Potasz, M. Korkusinski, and P. Hawrylak, *Graphene Quantum Dots* (Springer Berlin Heidelberg, Berlin Heidelberg, 2014).
[31] G. D. Mahan, *Many-Particle Physics* (Springer, Boston, MA, 1990).
[32] Laurent, Typical Operators in Tight Binding, Physics Stack Exchange, https://physics.stackexchange.com/q/53270.